Broadband light extraction from near-surface NV centers using crystalline-silicon antennas

Minjeong Kim[1], Maryam Zahedian[1], Wenxin Wu[1], Chengyu Fang[1], Zhaoning Yu[2], Raymond A. Wambold[1], Shenwei Yin[1], David A. Czaplewski[3], Jennifer T. Choy[1,2*], Mikhail A. Kats[1,2*]

[1] Department of Electrical and Computer Engineering, University of Wisconsin–Madison, Madison, WI 53706, USA

[2] Department of Physics, University of Wisconsin–Madison, Madison, WI 53706, USA

[3] Center for Nanoscale Materials, Argonne National Laboratory, Lemont, IL 60439, USA

[*] mkats@wisc.edu, jennifer.choy@wisc.edu

Abstract

We use crystalline silicon (Si) antennas to efficiently extract broadband single-photon fluorescence from shallow nitrogen-vacancy (NV) centers in diamond into free space. Our design features relatively easy-to-pattern high-index Si resonators on the diamond surface to boost photon extraction by overcoming total internal reflection and Fresnel reflection at the diamond-air interface, and providing modest Purcell enhancement, without etching or otherwise damaging the diamond surface. In simulations, ~20 times more single photons are collected from a single NV center compared to the case without the antenna; in experiments, we observe an enhancement of ~4 times, limited by spatial alignment between the NV and the antenna. Our approach can be readily applied to other color centers in diamond, and more generally to the extraction of light from quantum emitters in wide-bandgap materials.

Main text

Color centers in materials such as diamond,[1–3] silicon carbide,[4,5] and hexagonal boron nitride (h-BN)[6,7] are components of a host of emerging quantum technologies, including quantum

networking, [8–10] computation,[11–13] and sensing of electric and magnetic fields,[14,15] temperature,[16,17] strain,[18,19] and inertial motion.[20,21] Because these materials tend to have relatively high refractive index, light extraction from color centers is an important engineering problem; for example, only ~3% of the light emitted from negatively-charged nitrogen-vacancy (NV) centers (Fig. 1(a)) in (100) bulk diamond (refractive index $n \sim 2.4$) is transmitted through the diamond-air interface due to a combination of total internal reflection (TIR) and Fresnel reflection at the diamond-air interface (Fig. 1(b)).

Several solutions to the light-extraction problem have been explored, involving etching of the diamond surface, such as creating parabolic reflectors,[22] nanowires followed by metallization,[23] gratings,[24,25] and metasurfaces.[26] However, etching of the diamond surface can significantly affect the quality of NV centers just below the surface through material damage to the crystal or introduction of surface defects, but these near-surface NV centers are otherwise ideally suited for certain sensing applications such as high-resolution measurement of fields[27–29] and spin-based chemical sensing.[30] Furthermore, while etching of diamond is now reasonably well established,[31–33] it remains technically difficult and often requires a dedicated etching chamber. Therefore, the ideal solution for light extraction from NV centers in diamond and other color centers, especially for sensing applications, is to build structures on top of the diamond without etching or otherwise modifying the diamond surface. Two proposals for such light extractors have used adjoint optimization to design sophisticated high-index structures with small features and high aspect ratios that can be fabricated on top of a diamond surface: one experimentally realized structure in gallium phosphide,[34] and one proposal in silicon.[35] Here, we demonstrate relatively easy-to-design and single-step fabricated crystalline-silicon antennas that can efficiently extract and beam broadband fluorescence from NV centers, substantially increasing the number of single photons that can be collected with an objective lens in free space.

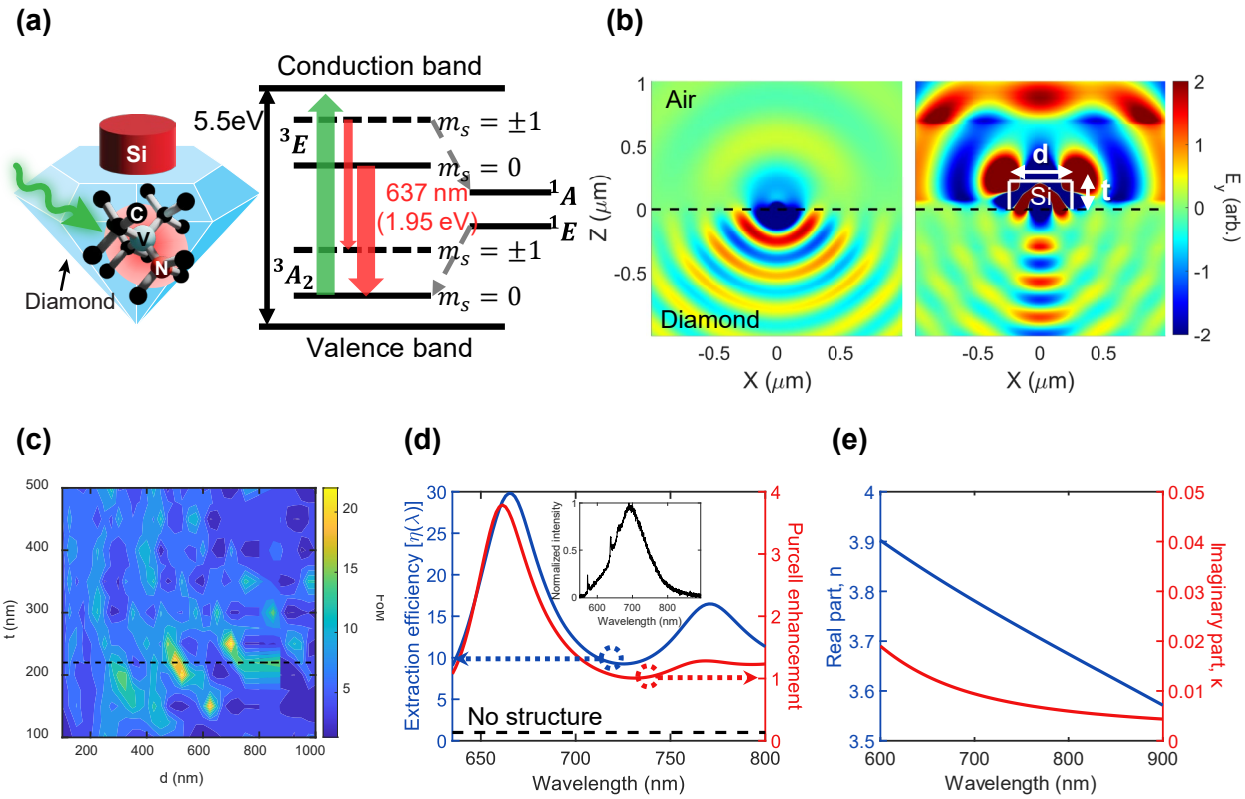

Figure 1. (a) Visualization of the NV$^-$ center in diamond and its energy-level diagram. The green arrow indicates the excitation, and the red arrows indicate the radiative transitions. (b) Snapshot of the simulated electric fields near a y-polarized dipole (parallel to interface) 10 nm below the interface between diamond and air, taken along a slice in the XZ plane at y = 0 (the center of the device and the y-coordinate of the NV) at a wavelength of 637 nm. The Si pillar is outlined. d: diameter of the pillar; t: thickness of the pillar. (c) Simulated color map of the figure of merit (FoM) with respect to the diameter (d) and thickness (t) of the Si pillar. The dotted line indicates the thickness of our device layer in this work (220 nm). (d) Simulated extraction efficiency [η(λ)] of the Si antenna for NV depths of 10 nm below the diamond/air interface (blue line) with Si pillar of d = 500 nm and t = 220 nm. Purcell enhancement (red line) of the Si pillar. Both extraction efficiency and Purcell enhancement are an average of two dipole orientations $[\bar{1}\bar{1}2]$ and $[1\bar{1}0]$. (Inset) Normalized photoluminescence spectrum of the NV center. (e) Real (blue) and imaginary (red) parts of the refractive index of crystalline Si, measured using variable-angle ellipsometry.

Fig. 1(a) shows our design, featuring a cylindrical pillar of single-crystal silicon (Si) positioned on the diamond surface, immediately above a sub-surface NV center at a depth of 5–15 nm. We utilized single-crystalline Si because its indirect bandgap results in sufficiently low absorption losses at wavelengths longer than ~600 nm, which correspond to the NV center spectrum, including the zero-phonon line and the phonon sideband. In contrast, polycrystalline and amorphous Si exhibit higher absorption coefficients at these wavelengths.[36] We validated our design with finite-difference time-domain (FDTD) simulations (Ansys Lumerical FDTD). In the

simulations (Fig. 1(b)), we positioned a y-polarized dipole 10 nm below the diamond-air interface (note that the dipole orientations with respect to the interface depend on the NV orientation and on the diamond cut[37]), observing that the majority of the emitted light remains confined within the diamond. However, incorporating a single-crystal Si pillar allows us to overcome total internal reflection (TIR) and Fresnel reflection due to the overlap of the near field from the emitter with the high-index Si resonator, thereby significantly enhancing light extraction from the dipole in the diamond (Fig. 1(b)). To optimize the diameter (d) and thickness (t) of the Si pillar for maximum light extraction across the NV emission spectrum, we use a spectrum-averaged figure of merit (FoM)[35]:

$$FoM = \frac{\int I_{NV}(\lambda) \cdot \eta(\lambda) d\lambda}{\int I_{NV}(\lambda) d\lambda} \quad (1)$$

Here, $I_{NV}(\lambda)$ is the normalized emission spectrum of the NV centers in bulk diamond,[38] and $\eta(\lambda)$ is the extraction efficiency of our device, defined as the ratio of the number of photons emitted into free space in the presence of the Si pillar to the number of photons emitted from the bare diamond surface without the Si pillar, accounting for both collection and Purcell enhancements. The bounds of the integral in Eq. (1) are set to 635–800 nm to encompass the NV zero-phonon line and phonon-sideband emission.

We swept over the Si pillar thickness (t) and diameter (d), finding several local maxima (Fig. 1(c)) and, in particular, a local maximum for $d \sim 500$ nm and $t \sim 220$ nm, yielding a FoM of approximately 20, indicating an increase of the optical power emitted into the air by a factor of 20 compared to the bare diamond surface. 220 nm is also a common silicon device-layer thickness used in silicon photonics,[39,40] and therefore crystalline Si membranes of this thickness are readily commercially available. The extraction efficiency $\eta(\lambda)$ and Purcell enhancement for the optimal Si pillar are shown in Fig. 1(d). The extraction efficiency is calculated by averaging the emitted power over two orthogonal electric dipoles at the NV location,[37] and the circular shape of the pillar ensures robustness to all four possible orientations of the NV in (100)-oriented diamond. The Purcell enhancement, representing the increased spontaneous emission rate experienced by the dipole in the cavity,[41] exceeds 2 for wavelengths in the 645–685 nm range.

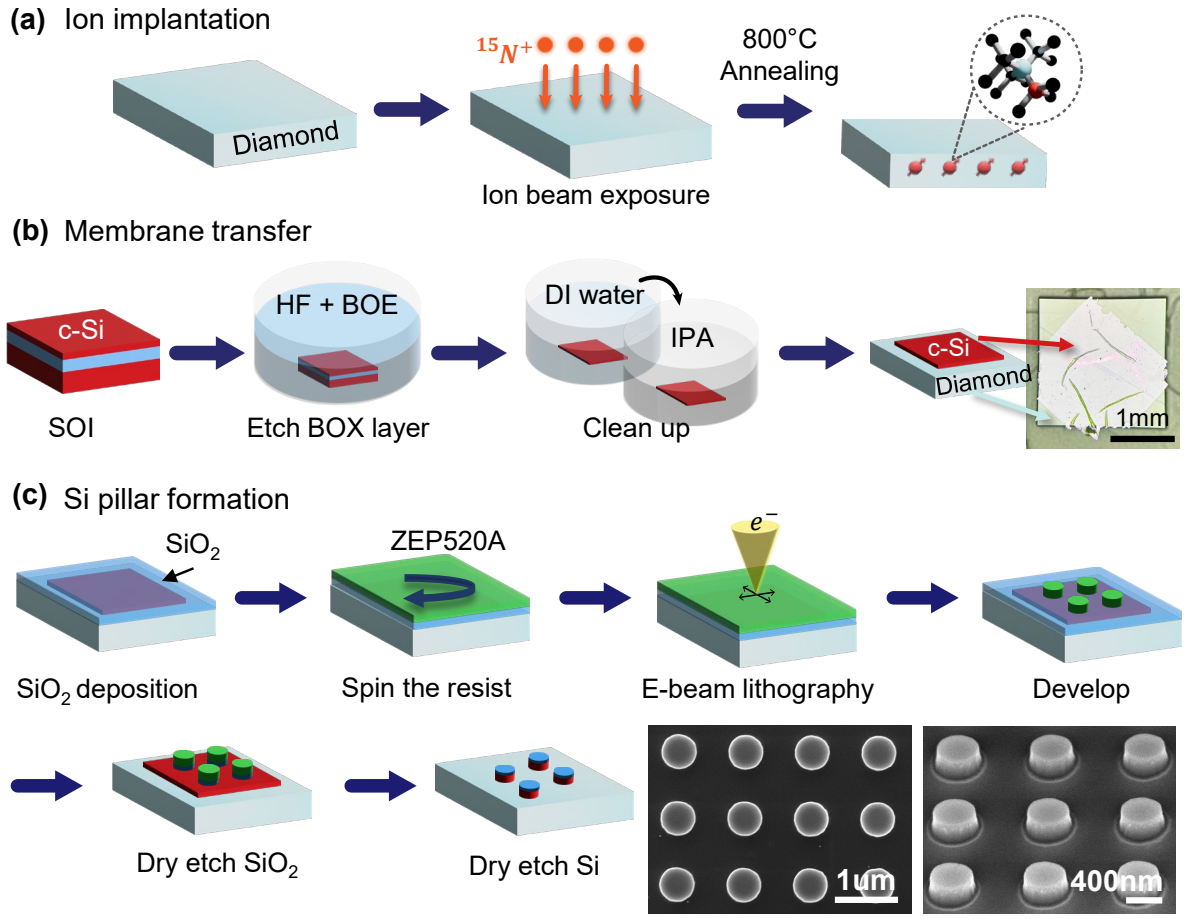

Figure 2. The fabrication procedure, along with photo and SEM images of the fabricated Si antennas. (a) Diamond sample is implanted with nitrogen ions at 4 keV and a dose of 2×10^9N/cm^2 and annealed to generate NV centers roughly 7 nm below the surface (Supporting Fig. S1). (b) The buried oxide (BOX) layer of the SOI piece is undercut using hydrogen fluoride (HF) and buffered oxide etchant (BOE) solution, and the Si membrane is wet-transferred onto the diamond substrate. The inset on the left is an optical microscope image of a c-Si membrane transferred to a 2 mm x 2 mm diamond sample. (c) An SiO_2 hard mask is deposited using plasma-enhanced chemical vapor deposition (PECVD). ZEP520A resist is spun onto the substrate, patterned via e-beam exposure, and developed. The SiO_2 and Si layers are then etched to form Si pillars (SEM images shown in the insets).

We fabricated the Si pillars by transferring a single-crystal silicon membrane from a silicon-on-insulator (SOI) wafer onto the diamond surface using an epitaxial lift-off technique.[42,43] A chemical vapor deposition (CVD) diamond substrate was ion-implanted with nitrogen ions, followed by vacuum annealing at 800 ˚C and tri-acid cleaning (Fig. 2(a)). The Si membrane was then released and transferred onto the diamond (Fig. 2(b)), and the structure was then defined using electron-beam lithography, etching of the hard mask, and Si etching (Fig. 2(c)). The SEM images

of the fabricated Si antennas are shown in Fig. 2(c). Detailed fabrication procedures are provided in the supporting information.

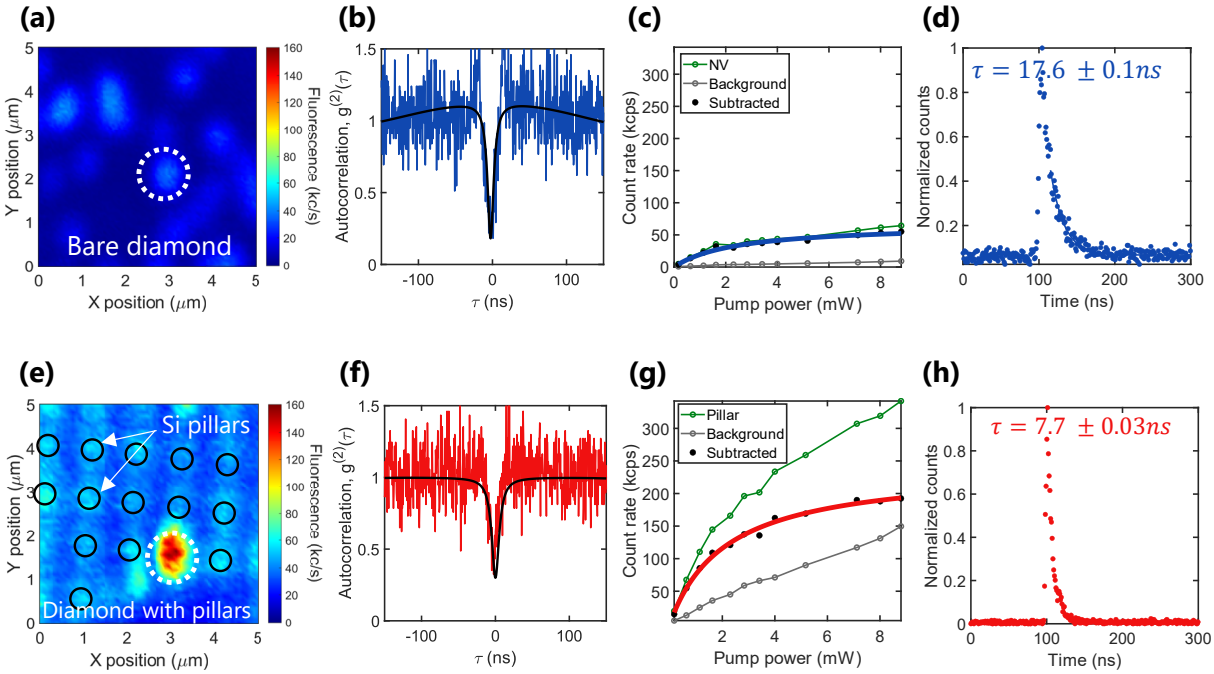

Figure 3. Comparison of NVs from bare diamond (a-d) and with Si antennas (e-h). The NV depth is similar between the two samples: ~9 nm in bare diamond in a-d, and ~7 nm in e-h. (a),(e) Confocal microscopy scans of a 5-μm by 5-μm region, with the circled regions (white dashed circles) representing the spots used for measurement and the black circles representing other nearby pillars. (b),(f) Autocorrelation function $g^2(\tau)$ for a single NV in the bare diamond (b), and underneath a Si pillar (f), showing anti-bunching at zero time delay τ, indicating emission of non-classical light. No background correction is performed. (c),(g) Saturation curves showing the total count rates as a function of pump power. Subtraction of the background from the total yields the isolated NV emission (black dots), which are fitted to a saturation model (blue and red lines, respectively). (d),(h) Normalized fluorescence decay for a single NV center in bare diamond, vs. with a Si antenna, fitted to an one-exponential model. The fits yield time constants of 17.59 ± 0.09 ns for single NVs in bare diamond (without Si antennas), and 7.65 ± 0.03 ns for single NVs underneath a Si antenna.

The fluorescence measurements were performed by exciting the sample with a continuous wave laser at 515 nm and collecting the NV center emission through the same objective (numerical aperture NA = 0.95), using a home-built confocal microscope. The fluorescence was focused onto a single-mode fiber connected to an avalanche photodiode (APD). Confocal scan images of each sample from the APD output are displayed in Fig. 3(a) and (e). Note that the ion implantation energy for the bare diamond was 6 keV, while for the diamond with Si antennas, it was 4 keV, resulting in slightly different NV depths of ~9 nm for the bare diamond and ~7 nm for the diamond with Si pillars, but this difference does not significantly affect the conclusion (Supporting Fig. S1). As shown in Fig. 3(a) and (e), the emission from the NV center with a Si antenna is clearly

enhanced compared to the bare diamond sample. To confirm single-photon characteristics of individual NV centers from both diamond samples, we measured the second-order autocorrelation function[44], $g^{(2)}(\tau) < 0.5$, without doing background subtraction, demonstrating that each contained a single-photon emitter without too much background (Fig. 3(b) and (f)). For both samples, we observed the characteristic optically detected magnetic resonance (ODMR) dip at 2.87 GHz[45] without an external magnetic field (Supporting Fig. S2).

Fluorescence intensity saturation curves of both samples were measured by varying the pump power (Fig. 3(c) and (g)). For the bare diamond, the background was measured in regions without NV centers, and for the diamond with Si antennas, the background was measured at a Si pillar without NV centers. The background-subtracted count rate, representing the NV fluorescence count rate, was fitted to the following saturation model[44]:

$$C(P) = \frac{C_{sat}}{1 + \frac{P_{sat}}{P}} \tag{2}$$

Here, C_{sat} is the saturated count rate, and P_{sat} is the saturation power and P is the laser power. We measured the C_{sat} of the NV center in the bare diamond to be ~67 kcps, while that for the NV center with the Si antenna is ~240 kcps, indicating a 3.6-fold increase. However, P_{sat} values are comparable in the two cases: P_{sat} of the NV center in the bare diamond is ~2.4 mW, and P_{sat} of the NV center with the Si antenna is ~2.1 mW. The normalized fluorescence count time traces were fitted to a one-exponential decay model, yielding time constants are 17.59 ± 0.09 ns for the bare diamond and 7.65 ± 0.03 ns for the diamond with Si antennas, indicating a 2.3-fold reduction in the lifetime in the presence of the Si antenna.

The 3.6-fold increase in measured broadband single-photon fluorescence is a significant improvement, but is considerably below the FoM ~ 20 observed in simulations. We believe that the discrepancy is due to misalignment of the Si pillar with the NV center, which is to be expected given the density of NVs in our sample, the density of the pillar array we fabricated, potential difference in NV depth,[46] and the lack of intentional alignment prior to the lithography (Supporting Fig. S3). In Supporting Fig. S4, we simulated the extraction FoM, Purcell factor, and the change in excitation intensity at the NV (leading to a different P_{sat}) due to the presence of the pillar, as a function of the displacement between the center of the pillar and the NV. We found that all of the

measured parameters in the experiment are consistent with a lateral displacement of 150–200 nm between the pillar and NV.

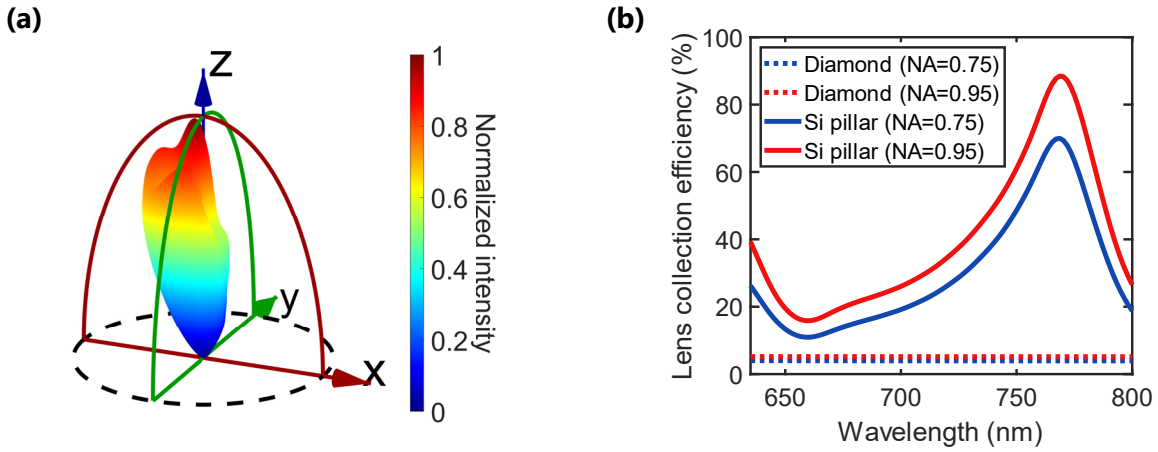

Figure 4. (a) Simulated far-field $|E|^2$ intensity distribution of the light emitted from NV center, averaged over the two dipole orientations $[\bar{1}\bar{1}2]$ and $[1\bar{1}0]$, at a depth of 10 nm passing through Si antenna. The plot is shown at a wavelength of 665 nm. (b) Collection efficiency of the emitted light by a lens, defined as the fraction of emitted power from Si antenna collected by a lens with a specific numerical aperture (NA). The lens used in the confocal microscope has an NA of 0.95.

In our previous work, where we generated a complex adjoint-optimized structure for light extraction,[35] the target performance was beaming into a specific Gaussian free-space mode of a certain size and orientation, which necessitated optimization over many structural degrees of freedom. However, the resulting structure was challenging to fabricate, and also was not rotationally symmetric, which meant that it was optimized for one particular NV orientation. Here, instead, we demonstrated that a much-simplified and rotationally symmetric design can achieve similar levels of light extraction, while sacrificing some beam quality (Fig. 4(a)). Despite the lower beam quality, optical collection can remain high—for example, for a free-space objective with NA of 0.95, as used in our confocal microscope setup, more than 40% of the broadband optical power emitted by the NV can be collected in free space (Fig. 4(b)).

In summary, we designed, fabricated, and characterized crystalline silicon (Si) antennas to enhance light extraction from nitrogen-vacancy (NV) centers in diamond. By leveraging the high refractive index of Si, our design achieves a simulated 20-fold enhancement compared to bare bulk diamond, while experimental measurements showed a 3.6-fold enhancement due to experimental misalignment between the NV and the antenna. Our approach avoids the etching of the diamond surface, which can increase surface roughness or alter chemical termination,[47–49] preserving the

integrity of near-surface NV centers, and making it well-suited for integrating nanophotonic structures with diamond. The Si platform can be further optimized and applied to other color centers, such as silicon-vacancy[50,51] and germanium-vacancy centers in diamond,[52,53] or for other quantum emitters in wide-bandgap materials.

Acknowledgements

The authors thank Robert Hamers discussions early on in the project. Contributions from MJ, ZY, and MAK are supported by the National Science Foundation under Grant No. CHE-1839174. Contributions from MZ and JTC are supported by the U.S. Department of Energy, Office of Science, Basic Energy Sciences under Award #DE-SC0020313. Contribution from WW is supported by the University of Wisconsin – Madison Office of the Vice Chancellor for Research and Graduate Education with funding from the Wisconsin Alumni Research Foundation. The majority of the fabrication work was performed at the Center for Nanoscale Materials, a U.S. Department of Energy Office of Science User Facility, was supported by the U.S. DOE, Office of Basic Energy Sciences, under Contract No. DE-AC02-06CH11357. The authors also acknowledge use of facilities and instrumentation at the UW-Madison Wisconsin Centers for Nanoscale Technology (wcnt.wisc.edu) partially supported by the NSF through the University of Wisconsin Materials Research Science and Engineering Center (DMR-2309000).

Methods

Diamond preparation

The 2 mm x 2 mm chemical vapor deposition (CVD) electronic-grade (100) single crystalline diamond substrates with less than 0.03 ppm nitrogen concentration were used to create NV centers. For the bare diamond, the sample was ion-implanted with nitrogen ions at an energy of 6 keV, followed by vacuum annealing at 800 °C and tri-acid cleaning with equal parts nitric (HNO_3), perchloric ($HClO_4$), and sulfuric acids (H_2SO_4). For the diamond with Si antennas, a similar substrate underwent strain relief etching using inductively coupled plasma reactive-ion etching

(ICP-RIE, Plasma-Therm),[47] ion implantation at an energy of 4 keV, followed by vacuum annealing at 800 °C and tri-acid cleaning.

Device fabrication

To confirm the optical properties of the crystalline Si from SOI wafers, we measured real and imaginary parts of refractive index of the device layer from an SOI wafer using variable-angle spectroscopic ellipsometry (J.A. Woollam V-VASE) (Fig. 1(e)). Then, SOI wafers with a 220 nm layer of single-crystal silicon were diced, cleaned, and the silicon membranes were released using a mixture of hydrogen fluoride (HF) and buffered oxide etchant (BOE). The membranes were then transferred onto the diamond substrate (Fig. 2(b)). A ~27 nm layer of SiO_2 was deposited onto the silicon membrane using PECVD as a hard mask. Arrays of circular patterns with a diameter of 500 nm were defined using electron-beam lithography. These patterns were transferred into the hard mask using ICP-RIE (Oxford) with CHF_3 and O_2. Finally, 220 nm tall silicon antennas were created using HBr and O_2 etching (Fig. 2(c)). The SiO_2 hard mask was not removed, and is not expected to significantly affect the optical properties due to its low index and small thickness (Supporting Fig. S6).

Measurement

Confocal scans, ODMR, and lifetime measurements were performed using a custom-built confocal fluorescence microscope. NV centers were excited with a 515 nm laser (Omicron LuxX 515-100), and emission was collected using two APDs (Laser Components COUNT-100N-FC) with filters through a 0.95 NA air objective at ~2.3 mW. A fast-steering mirror (FSM-300-NM) was used for scanning, Continuous-wave 515 nm laser was used for confocal scans and ODMR, with fluorescence images captured using Qudi software, scanning 5 µm x 5 µm regions at 0.1 µm resolution. For ODMR, microwaves were applied via a printed circuit board (PCB), sweeping from 2.83 GHz to 2.92 GHz. Lifetime measurements were conducted using ~5 ns pulse excitations generated via digital control of the laser using a Pulse Streamer (Swabian instruments), with time-gated measurements recorded by a Time Tagger (Swabian instruments) at ~2.3 mW (CW mode).

References

(1) Schirhagl, R.; Chang, K.; Loretz, M.; Degen, C. L. Nitrogen-Vacancy Centers in Diamond: Nanoscale Sensors for Physics and Biology. *Annu Rev Phys Chem* **2014**, *65* (Volume 65,

2014), 83–105. https://doi.org/10.1146/ANNUREV-PHYSCHEM-040513-103659/CITE/REFWORKS.

(2) Aharonovich, I.; Greentree, A. D.; Prawer, S. Diamond Photonics. *Nature Photonics*. July 2011, pp 397–405. https://doi.org/10.1038/nphoton.2011.54.

(3) Jelezko, F.; Wrachtrup, J. Single Defect Centres in Diamond: A Review. *Physica Status Solidi (A) Applications and Materials Science*. October 2006, pp 3207–3225. https://doi.org/10.1002/pssa.200671403.

(4) Castelletto, S.; Boretti, A. Silicon Carbide Color Centers for Quantum Applications. *JPhys Photonics*. IOP Publishing Ltd March 6, 2020. https://doi.org/10.1088/2515-7647/ab77a2.

(5) Lukin, D. M.; Guidry, M. A.; Vučković, J. Integrated Quantum Photonics with Silicon Carbide: Challenges and Prospects. *PRX Quantum* **2020**, *1* (2). https://doi.org/10.1103/PRXQuantum.1.020102.

(6) Caldwell, J. D.; Aharonovich, I.; Cassabois, G.; Edgar, J. H.; Gil, B.; Basov, D. N. Photonics with Hexagonal Boron Nitride. *Nature Reviews Materials*. Nature Publishing Group August 1, 2019, pp 552–567. https://doi.org/10.1038/s41578-019-0124-1.

(7) Abdi, M.; Chou, J. P.; Gali, A.; Plenio, M. B. Color Centers in Hexagonal Boron Nitride Monolayers: A Group Theory and Ab Initio Analysis. *ACS Photonics* **2018**, *5* (5), 1967–1976. https://doi.org/10.1021/acsphotonics.7b01442.

(8) Pompili, M.; Hermans, S. L. N.; Baier, S.; Beukers, H. K. C.; Humphreys, P. C.; Schouten, R. N.; Vermeulen, R. F. L.; Tiggelman, M. J.; Dos, L.; Martins, S.; Dirkse, B.; Wehner, S.; Hanson, R. *Realization of a Multinode Quantum Network of Remote Solid-State Qubits*; 2021; Vol. 372. https://www.science.org.

(9) Bernien, H.; Childress, L.; Robledo, L.; Markham, M.; Twitchen, D.; Hanson, R. Two-Photon Quantum Interference from Separate Nitrogen Vacancy Centers in Diamond. *Phys Rev Lett* **2012**, *108* (4). https://doi.org/10.1103/PhysRevLett.108.043604.

(10) Acosta, V. M.; Santori, C.; Faraon, A.; Huang, Z.; Fu, K. M. C.; Stacey, A.; Simpson, D. A.; Ganesan, K.; Tomljenovic-Hanic, S.; Greentree, A. D.; Prawer, S.; Beausoleil, R. G. Dynamic Stabilization of the Optical Resonances of Single Nitrogen-Vacancy Centers in Diamond. *Phys Rev Lett* **2012**, *108* (20). https://doi.org/10.1103/PhysRevLett.108.206401.

(11) Wrachtrup, J.; Kilin, S. Ya.; Nizovtsev, A. P. Quantum Computation Using the C-13 Nuclear Spins near the Single NV Defect Center in Diamond. *Opt Spectrosc* **2001**, *91* (3), 429–437.

(12) Weber, J. R.; Koehl, W. F.; Varley, J. B.; Janotti, A.; Buckley, B. B.; Van De Walle, C. G.; Awschalom, D. D. Quantum Computing with Defects. *Proc Natl Acad Sci U S A* **2010**, *107* (19), 8513–8518. https://doi.org/10.1073/pnas.1003052107.

(13) Ladd, T. D.; Jelezko, F.; Laflamme, R.; Nakamura, Y.; Monroe, C.; O'Brien, J. L. Quantum Computers. *Nature*. 2010, pp 45–53. https://doi.org/10.1038/nature08812.

(14) Hong, S.; Grinolds, M. S.; Pham, L. M.; Le Sage, D.; Luan, L.; Walsworth, R. L.; Yacoby, A. Nanoscale Magnetometry with NV Centers in Diamond. *MRS Bulletin*. February 2013, pp 155–161. https://doi.org/10.1557/mrs.2013.23.

(15) Rondin, L.; Tetienne, J. P.; Hingant, T.; Roch, J. F.; Maletinsky, P.; Jacques, V. Magnetometry with Nitrogen-Vacancy Defects in Diamond. *Reports on Progress in Physics*. Institute of Physics Publishing 2014. https://doi.org/10.1088/0034-4885/77/5/056503.

(16) Acosta, V. M.; Bauch, E.; Ledbetter, M. P.; Waxman, A.; Bouchard, L. S.; Budker, D. Temperature Dependence of the Nitrogen-Vacancy Magnetic Resonance in Diamond. *Phys Rev Lett* **2010**, *104* (7). https://doi.org/10.1103/PhysRevLett.104.070801.

(17) Plakhotnik, T.; Doherty, M. W.; Cole, J. H.; Chapman, R.; Manson, N. B. All-Optical Thermometry and Thermal Properties of the Optically Detected Spin Resonances of the NV- Center in Nanodiamond. *Nano Lett* **2014**, *14* (9), 4989–4996. https://doi.org/10.1021/nl501841d.

(18) Ovartchaiyapong, P.; Lee, K. W.; Myers, B. A.; Jayich, A. C. B. Dynamic Strain-Mediated Coupling of a Single Diamond Spin to a Mechanical Resonator. *Nat Commun* **2014**, *5*. https://doi.org/10.1038/ncomms5429.

(19) Doherty, M. W.; Struzhkin, V. V.; Simpson, D. A.; McGuinness, L. P.; Meng, Y.; Stacey, A.; Karle, T. J.; Hemley, R. J.; Manson, N. B.; Hollenberg, L. C. L.; Prawer, S. Electronic Properties and Metrology Applications of the Diamond NV - Center under Pressure. *Phys Rev Lett* **2014**, *112* (4). https://doi.org/10.1103/PhysRevLett.112.047601.

(20) Soshenko, V. V.; Bolshedvorskii, S. V.; Rubinas, O.; Sorokin, V. N.; Smolyaninov, A. N.; Vorobyov, V. V.; Akimov, A. V. Nuclear Spin Gyroscope Based on the Nitrogen Vacancy Center in Diamond. *Phys Rev Lett* **2021**, *126* (19). https://doi.org/10.1103/PhysRevLett.126.197702.

(21) Ledbetter, M. P.; Jensen, K.; Fischer, R.; Jarmola, A.; Budker, D. Gyroscopes Based on Nitrogen-Vacancy Centers in Diamond. *Phys Rev A* **2012**, *86* (5). https://doi.org/10.1103/PhysRevA.86.052116.

(22) Wan, N. H.; Shields, B. J.; Kim, D.; Mouradian, S.; Lienhard, B.; Walsh, M.; Bakhru, H.; Schröder, T.; Englund, D. Efficient Extraction of Light from a Nitrogen-Vacancy Center in a Diamond Parabolic Reflector. *Nano Lett* **2018**, *18* (5), 2787–2793. https://doi.org/10.1021/acs.nanolett.7b04684.

(23) Choy, J. T.; Hausmann, B. J. M.; Babinec, T. M.; Bulu, I.; Khan, M.; Maletinsky, P.; Yacoby, A.; Loňcar, M. Enhanced Single-Photon Emission from a Diamond-Silver Aperture. *Nat Photonics* **2011**, *5* (12), 738–743. https://doi.org/10.1038/nphoton.2011.249.

(24) Li, L.; Chen, E. H.; Zheng, J.; Mouradian, S. L.; Dolde, F.; Schröder, T.; Karaveli, S.; Markham, M. L.; Twitchen, D. J.; Englund, D. Efficient Photon Collection from a Nitrogen Vacancy Center in a Circular Bullseye Grating. *Nano Lett* **2015**, *15* (3), 1493–1497. https://doi.org/10.1021/NL503451J/SUPPL_FILE/NL503451J_SI_001.PDF.

(25) Choy, J. T.; Bulu, I.; Hausmann, B. J. M.; Janitz, E.; Huang, I. C.; Lončar, M. Spontaneous Emission and Collection Efficiency Enhancement of Single Emitters in Diamond via Plasmonic Cavities and Gratings. *Appl Phys Lett* **2013**, *103* (16). https://doi.org/10.1063/1.4817397.

(26) Huang, T. Y.; Grote, R. R.; Mann, S. A.; Hopper, D. A.; Exarhos, A. L.; Lopez, G. G.; Klein, A. R.; Garnett, E. C.; Bassett, L. C. A Monolithic Immersion Metalens for Imaging Solid-State Quantum Emitters. *Nat Commun* **2019**, *10* (1). https://doi.org/10.1038/s41467-019-10238-5.

(27) Taylor, J. M.; Cappellaro, P.; Childress, L.; Jiang, L.; Budker, D.; Hemmer, P. R.; Yacoby, A.; Walsworth, R.; Lukin, M. D. High-Sensitivity Diamond Magnetometer with Nanoscale Resolution. *Nat Phys* **2008**, *4* (10), 810–816. https://doi.org/10.1038/nphys1075.

(28) Bernardi, E.; Nelz, R.; Sonusen, S.; Neu, E. Nanoscale Sensing Using Point Defects in Single-Crystal Diamond: Recent Progress on Nitrogen Vacancy Center-Based Sensors. *Crystals (Basel)* **2017**, *7* (5). https://doi.org/10.3390/cryst7050124.

(29) Glenn, D. R.; Bucher, D. B.; Lee, J.; Lukin, M. D.; Park, H.; Walsworth, R. L. High-Resolution Magnetic Resonance Spectroscopy Using a Solid-State Spin Sensor. *Nature* **2018**, *555* (7696), 351–354. https://doi.org/10.1038/nature25781.

(30) Bachman, B. F.; Jones, Z. R.; Jaffe, G. R.; Salman, J.; Wambold, R.; Yu, Z.; Choy, J. T.; Kolkowitz, S. J.; Eriksson, M. A.; Kats, M. A.; Hamers, R. J. High-Density Covalent Grafting of Spin-Active Molecular Moieties to Diamond Surfaces. *Langmuir* **2021**, *37* (30), 9222–9231. https://doi.org/10.1021/ACS.LANGMUIR.1C01425/ASSET/IMAGES/LARGE/LA1C01425_0008.JPEG.

(31) Cui, S.; Greenspon, A. S.; Ohno, K.; Myers, B. A.; Jayich, A. C. B.; Awschalom, D. D.; Hu, E. L. Reduced Plasma-Induced Damage to near-Surface Nitrogen-Vacancy Centers in Diamond. *Nano Lett* **2015**, *15* (5), 2887–2891. https://doi.org/10.1021/acs.nanolett.5b00457.

(32) Nagai, M.; Nakanishi, K.; Takahashi, H.; Kato, H.; Makino, T.; Yamasaki, S.; Matsumoto, T.; Inokuma, T.; Tokuda, N. Anisotropic Diamond Etching through Thermochemical Reaction between Ni and Diamond in High-Temperature Water Vapour. *Sci Rep* **2018**, *8* (1). https://doi.org/10.1038/s41598-018-25193-2.

(33) Hicks, M. L.; Pakpour-Tabrizi, A. C.; Jackman, R. B. Polishing, Preparation and Patterning of Diamond for Device Applications. *Diam Relat Mater* **2019**, *97*. https://doi.org/10.1016/j.diamond.2019.05.010.

(34) Chakravarthi, S.; Chao, P.; Chao, P.; Pederson, C.; Molesky, S.; Ivanov, A.; Hestroffer, K.; Hatami, F.; Rodriguez, A. W.; Fu, K.-M. C. Inverse-Designed Photon Extractors for Optically Addressable Defect Qubits. *Optica, Vol. 7, Issue 12, pp. 1805-1811* **2020**, *7* (12), 1805–1811. https://doi.org/10.1364/OPTICA.408611.

(35) Wambold, R. A.; Yu, Z.; Xiao, Y.; Bachman, B.; Jaffe, G.; Kolkowitz, S.; Choy, J. T.; Eriksson, M. A.; Hamers, R. J.; Kats, M. A. Adjoint-Optimized Nanoscale Light Extractor for Nitrogen-Vacancy Centers in Diamond. *Nanophotonics* **2020**, *10* (1), 393–401. https://doi.org/10.1515/nanoph-2020-0387.

(36) Sell, D.; Yang, J.; Doshay, S.; Zhang, K.; Fan, J. A. Visible Light Metasurfaces Based on Single-Crystal Silicon. *ACS Photonics* **2016**, *3* (10), 1919–1925. https://doi.org/10.1021/acsphotonics.6b00436.

(37) Zahedian, M.; Liu, J.; Vidrio, R.; Kolkowitz, S.; Choy, J. T. Modeling of Radiative Emission from Shallow Color Centers in Single Crystalline Diamond. *Laser Photon Rev* **2023**, *17* (4). https://doi.org/10.1002/lpor.202200529.

(38) Albrecht, R.; Bommer, A.; Deutsch, C.; Reichel, J.; Becher, C. Coupling of a Single Nitrogen-Vacancy Center in Diamond to a Fiber-Based Microcavity. *Phys Rev Lett* **2013**, *110* (24). https://doi.org/10.1103/PhysRevLett.110.243602.

(39) Halir, R.; Bock, P. J.; Cheben, P.; Ortega-Moñux, A.; Alonso-Ramos, C.; Schmid, J. H.; Lapointe, J.; Xu, D. X.; Wangüemert-Pérez, J. G.; Molina-Fernández, Í.; Janz, S. Waveguide Sub-Wavelength Structures: A Review of Principles and Applications. *Laser and Photonics Reviews*. Wiley-VCH Verlag January 1, 2015, pp 25–49. https://doi.org/10.1002/lpor.201400083.

(40) Lim, A. E. J.; Song, J.; Fang, Q.; Li, C.; Tu, X.; Duan, N.; Chen, K. K.; Tern, R. P. C.; Liow, T. Y. Review of Silicon Photonics Foundry Efforts. *IEEE Journal of Selected Topics in Quantum Electronics* **2014**, *20* (4). https://doi.org/10.1109/JSTQE.2013.2293274.

(41) Purcell, E. M. Proceedings of the American Physical Society : Spontaneous Emission Probabilities at Ratio Frequencies. *Physical Review* **1946**, *69* (11–12), 674–674. https://doi.org/10.1103/PhysRev.69.674.

(42) Konagai, M.; Sugimoto, M.; Takahashi, K. *HIGH EFFICIENCY GaAs THIJ'~4FILM SOLAR CELLS BY PEELED FiLM TECHNOLOGY*; 1978; Vol. 45.

(43) Cheng, C. W.; Shiu, K. T.; Li, N.; Han, S. J.; Shi, L.; Sadana, D. K. Epitaxial Lift-off Process for Gallium Arsenide Substrate Reuse and Flexible Electronics. *Nat Commun* **2013**, *4*. https://doi.org/10.1038/ncomms2583.

(44) Kurtsiefer, C.; Mayer, S.; Zarda, P.; Weinfurter, H. Stable Solid-State Source of Single Photons. *Phys Rev Lett* **2000**, *85* (2), 290–293. https://doi.org/10.1103/PhysRevLett.85.290.

(45) Gruber, A.; Dräbenstedt, A.; Tietz, C.; Fleury, L.; Wrachtrup, J.; Borczyskowski, C. von. Scanning Confocal Optical Microscopy and Magnetic Resonance on Single Defect Centers. *Science (1979)* **1997**, *276* (5321), 2012–2014. https://doi.org/10.1126/science.276.5321.2012.

(46) Pham, L. M.; Devience, S. J.; Casola, F.; Lovchinsky, I.; Sushkov, A. O.; Bersin, E.; Lee, J.; Urbach, E.; Cappellaro, P.; Park, H.; Yacoby, A.; Lukin, M.; Walsworth, R. L. NMR

Technique for Determining the Depth of Shallow Nitrogen-Vacancy Centers in Diamond. *Phys Rev B* **2016**, *93* (4). https://doi.org/10.1103/PhysRevB.93.045425.

(47) Sangtawesin, S.; Dwyer, B. L.; Srinivasan, S.; Allred, J. J.; Rodgers, L. V. H.; De Greve, K.; Stacey, A.; Dontschuk, N.; O'Donnell, K. M.; Hu, D.; Evans, D. A.; Jaye, C.; Fischer, D. A.; Markham, M. L.; Twitchen, D. J.; Park, H.; Lukin, M. D.; De Leon, N. P. Origins of Diamond Surface Noise Probed by Correlating Single-Spin Measurements with Surface Spectroscopy. *Phys Rev X* **2019**, *9* (3). https://doi.org/10.1103/PhysRevX.9.031052.

(48) Ofori-Okai, B. K.; Pezzagna, S.; Chang, K.; Loretz, M.; Schirhagl, R.; Tao, Y.; Moores, B. A.; Groot-Berning, K.; Meijer, J.; Degen, C. L. Spin Properties of Very Shallow Nitrogen Vacancy Defects in Diamond. *Phys Rev B Condens Matter Mater Phys* **2012**, *86* (8). https://doi.org/10.1103/PhysRevB.86.081406.

(49) de Leon, N. P.; Itoh, K. M.; Kim, D.; Mehta, K. K.; Northup, T. E.; Paik, H.; Palmer, B. S.; Samarth, N.; Sangtawesin, S.; Steuerman, D. W. Materials Challenges and Opportunities for Quantum Computing Hardware. *Science*. American Association for the Advancement of Science April 16, 2021. https://doi.org/10.1126/science.abb2823.

(50) Ondič, L.; Varga, M.; Hruška, K.; Fait, J.; Kapusta, P. Enhanced Extraction of Silicon-Vacancy Centers Light Emission Using Bottom-Up Engineered Polycrystalline Diamond Photonic Crystal Slabs. *ACS Nano* **2017**, *11* (3), 2972–2981. https://doi.org/10.1021/acsnano.6b08412.

(51) Chakravarthi, S.; Yama, N. S.; Abulnaga, A.; Huang, D.; Pederson, C.; Hestroffer, K.; Hatami, F.; de Leon, N. P.; Fu, K. M. C. Hybrid Integration of GaP Photonic Crystal Cavities with Silicon-Vacancy Centers in Diamond by Stamp-Transfer. *Nano Lett* **2023**, *23* (9), 3708–3715. https://doi.org/10.1021/acs.nanolett.2c04890.

(52) Iwasaki, T.; Ishibashi, F.; Miyamoto, Y.; Doi, Y.; Kobayashi, S.; Miyazaki, T.; Tahara, K.; Jahnke, K. D.; Rogers, L. J.; Naydenov, B.; Jelezko, F.; Yamasaki, S.; Nagamachi, S.; Inubushi, T.; Mizuochi, N.; Hatano, M. Germanium-Vacancy Single Color Centers in Diamond. *Sci Rep* **2015**, *5*. https://doi.org/10.1038/srep12882.

(53) Bhaskar, M. K.; Sukachev, D. D.; Sipahigil, A.; Evans, R. E.; Burek, M. J.; Nguyen, C. T.; Rogers, L. J.; Siyushev, P.; Metsch, M. H.; Park, H.; Jelezko, F.; Lončar, M.; Lukin, M. D. Quantum Nonlinear Optics with a Germanium-Vacancy Color Center in a Nanoscale Diamond Waveguide. *Phys Rev Lett* **2017**, *118* (22). https://doi.org/10.1103/PhysRevLett.118.223603.

Supporting Information:

Broadband light extraction from near-surface NV centers using crystalline-silicon antennas

Minjeong Kim[1], Maryam Zahedian[1], Wenxin Wu[1], Chengyu Fang[1], Zhaoning Yu[2], Raymond A. Wambold[1], Shenwei Yin[1], David A. Czaplewski[3], Jennifer T. Choy[1,2*], Mikhail A. Kats[1,2*]

[1] Department of Electrical and Computer Engineering, University of Wisconsin–Madison, Madison, WI 53706, USA

[2] Department of Physics, University of Wisconsin–Madison, Madison, WI 53706, USA

[3] Center for Nanoscale Materials, Argonne National Laboratory, Lemont, IL 60439, USA

[*] mkats@wisc.edu, jennifer.choy@wisc.edu

Experimental section:

Ion implantation and diamond preparation

NV centers in the bare (100) single crystalline diamond:

A 2 mm x 2 mm piece of electronic-grade diamond with a nitrogen concentration of less than 0.03 ppm was used as the reference sample. The diamond underwent tri-acid cleaning with a solution consisting of equal parts nitric, perchloric, and sulfuric acids, and was then implanted with a fluence of 2×10^9 N/cm² and an implantation energy of 6 keV. The implanted diamond was then annealed under high vacuum (<10^6 Torr) at 800 °C to form NV centers centered a depth of ~9.4 nm (Supporting Fig. S1), followed by another tri-acid cleaning.

NV centers in (100) single crystalline diamond with Si antenna:

A 2 mm x 2 mm piece of electronic-grade diamond with a nitrogen concentration of less than 0.03 ppm (ELSC20, Thorlabs) was used for implantation. The sample underwent strain-relief etching using inductively coupled plasma reactive ion etching (ICP-RIE, Plasma-Therm), resulting in the removal of ~5 μm from the surface, followed by tri-acid cleaning. Ion-beam exposure with a fluence of 2×10^9 N/cm^2 and an implantation energy of 4 keV was performed. The implanted

diamond was annealed under high vacuum (<10^6 Torr) at 800 °C to create NV centers centered at ~7 nm (Supporting Fig. S1), based on SRIM simulation. Post annealing, tri-acid cleaning was conducted to remove the graphitized layer formed during annealing.

Device fabrication

Preparation of silicon membrane and transfer to diamond:

SOI wafers, featuring a 220 nm layer of single-crystal silicon, were diced into 1 mm x 1 mm squares. These pieces were cleaned in Remover 1165 at 100 °C for 5 minutes, followed by ultrasonication in acetone and isopropanol (IPA) for 5 minutes each. The SOI piece was then immersed in a 1:1 mixture of 49% hydrogen fluoride (HF) and 20:1 buffered oxide etchant (BOE) for 17 hours to release the silicon (Si) membrane. The floating Si membrane was transferred to a 6:1 BOE solution for 4 hours to remove any remaining SiO_2 residue, followed by thorough rinsing in deionized (DI) water and IPA to clean up any HF residue. The ion-implanted diamond was cleaned in acetone and IPA for 5 minutes each. The silicon membrane was scooped up with a diamond and dried with a nitrogen gun. The diamond with the transferred silicon membrane was then placed on a hot plate at 90 °C for 10 minutes, followed by rapid thermal annealing (RTA) at 350 °C in nitrogen for 5 minutes.

Patterning and fabrication of Si antennas:

The diamond with the transferred silicon membrane was cleaned in a piranha solution, 4:1 mixture of sulfuric acid (H_2SO_4) and hydrogen peroxide (H_2O_2) for 2 minutes, followed by ultrasonication in acetone and IPA for 2 minutes each. A ~27 nm layer of SiO_2 was deposited onto the silicon membrane using PECVD (Oxford Plasmalab 100). A 1:1 mixture of ZEP520A and anisole was spin-coated onto the sample and baked at 150 °C for 3 minutes. Arrays of circular patterns were then defined using a JEOL JBX-8100FS electron-beam lithography system at 100 keV. After exposure, the pattern was developed in n-Amyl acetate for 1 minute and then rinsed with IPA. The features were defined in the hard mask using inductively coupled plasma reactive-ion etching (ICP-RIE, Oxford) with CHF_3 and O_2. Finally, 220 nm tall silicon antennas were created using HBr and O_2 etching, and any remaining resist residue was removed with an O_2 plasma treatment.

Characterization

Confocal scans, optically detected magnetic resonance (ODMR), and lifetime measurements for diamond samples were performed using a home-built confocal fluorescence microscope. NV centers were excited by a 515 nm green laser (Omicron LuxX 515-100), and the emitted fluorescence was collected using two avalanche photodiodes (APD, Laser Components COUNT-100N-FC) after passing through a 552 nm and 660 nm edge dichroic beam splitter and a 650 nm long pass filter. Both excitation and emission were focused and collected by an air objective with a numerical aperture (NA) of 0.95 (CFI Plan Apo Lambda 40XC/0.95 Air). A fast-steering mirror (FSM-300-NM) was employed to scan the laser beam across the sample. For lifetime measurements, pulsed excitation with ~5 ns pulses generated by a Pulse Streamer was utilized, and time-gated measurements were controlled by a Time Tagger at a power of ~2.3 mW (measured in continuous wave (CW) mode). For the confocal scans, ODMRs, and autocorrelation measurements, the excitation was a CW 515 nm laser. Fluorescence images were captured using the open-source Qudi software, scanning regions of 5 µm x 5 µm with a spatial resolution of 0.1 µm at a power of ~2.3 mW (measured in CW mode). Microwaves generated by a microwave/RF signal generator (Berkely Nucleonics, Model 835) were delivered to the sample via a printed circuit board (PCB), with the diamond mounted on the microwave resonator using carbon tape. During the ODMR experiments, the microwave frequency was swept from 2.83 GHz to 2.92, with the microwave CW power was set to −15 dBm.

NV center depths:

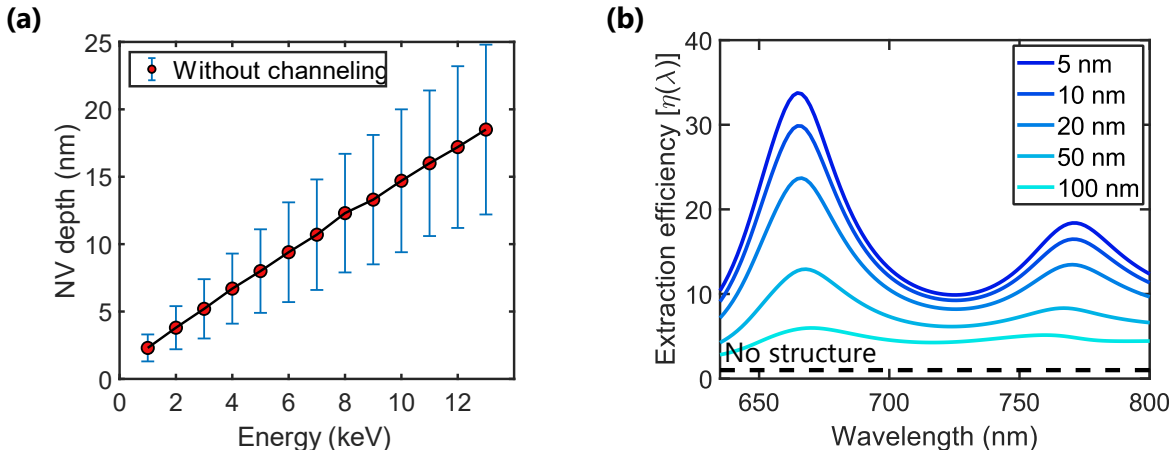

Figure S1. (a) Stopping and range of ions in matter (SRIM) simulation, performed assuming no channeling, of nitrogen ions implanted into diamond. (b) Extraction efficiency [η(λ)] of Si antennas as function of NV depths.

We estimated NV center penetration depth based on nitrogen ion implantation energy using stopping and range of ions in matter (SRIM) simulations for energies ranging from 1 keV to 13 keV. Diamond samples were ion implanted at 4 keV (bare diamond) and 6 keV (diamond with Si antennas). As shown in Fig. S1(a), 4 keV implantation yields an NV center penetration depth centered at ~7 nm, while 6 keV results in a depth centered at ~9.4 nm. Fig. S1(b) shows the extraction efficiency of Si antennas with a diameter of 500 nm and a height of 220 nm as a function of NV center depth, indicating no significant difference in extraction efficiency for NV depths between 5 nm and 10 nm.

Optically detected magnetic resonance (ODMR):

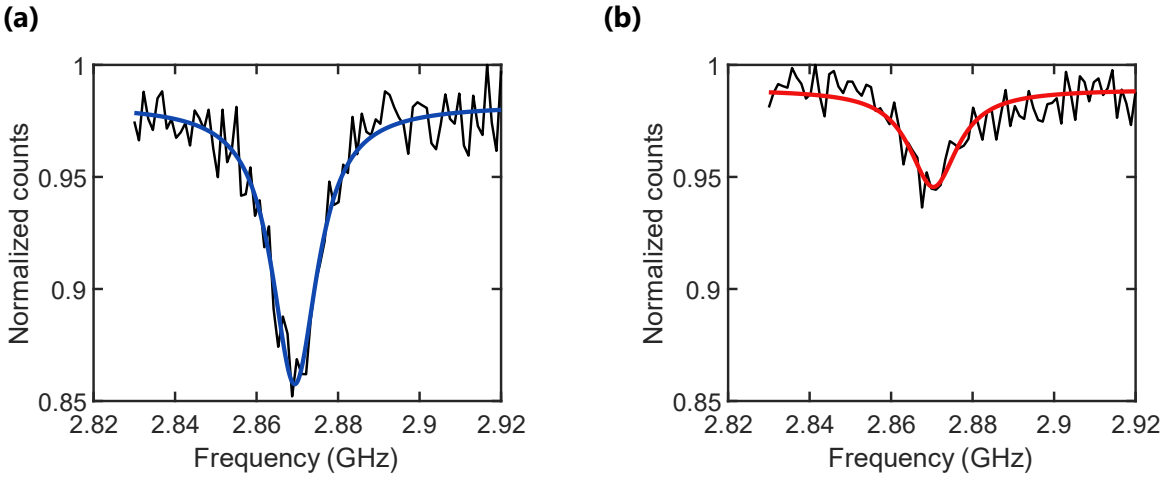

Figure S2. Optically detected magnetic resonance (ODMR), showing a dip at 2.87 GHz. (a) Result from bare diamond and (b) Result from Si antennas on diamond.

The ODMR spectra of the NV centers were measured by sweeping the microwave source over the NV center splitting between the $m_s = 0$ and $m_s = \pm 1$ ground-state levels (Fig. 1(a)) without an external magnetic field. Each spectrum shows a characteristic dip at 2.87 GHz. The difference in ODMR contrasts is likely attributed to variations in experimental parameters.

Possible fabrication errors:

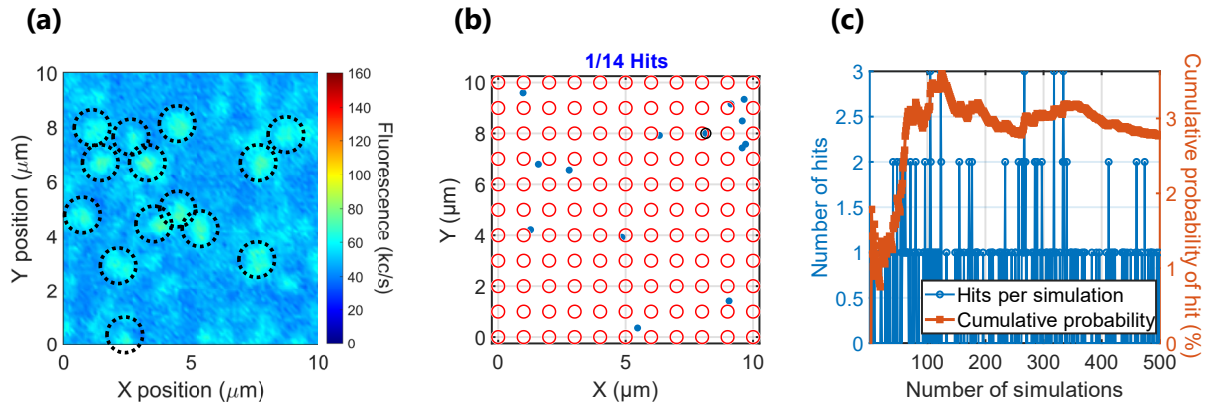

Figure S3. (a) Confocal scan of diamond ion-implanted with 4 keV before Si membrane transfer, with black circles representing potential single NVs. (b) Simulation of a square array of Si pillars (500 nm diameter, 1 μm period) showing the probability of a Si pillar being positioned on top of NVs (blue dots). A 'hit' is defined as a scenario where the distance between the center of a Si pillar and an NV is less than 150 nm. (c) Simulated cumulative probability of achieving a hit, based on 1000 iterations.

Prior to fabrication, we performed confocal microscopy on a diamond sample ion-implanted at 4 keV, identifying 14 potential single NV centers within a 10 μm × 10 μm area. Using this information, we simulated a square array of Si pillars—each 500 nm in diameter with a 1 μm period—randomly positioned on the NV centers. A 'hit' was defined as an instance where the distance between the center of a Si pillar and an NV center is less than 150 nm. After 1000 simulation iterations, we found an ~8% probability of a Si pillar aligning with an NV center within a 10 μm × 10 μm area. This suggests that across 13 scans of such 10 μm × 10 μm regions with similar densities as the confocal scan in Fig. S3(a), at least one Si pillar is likely to be properly aligned with an NV center.

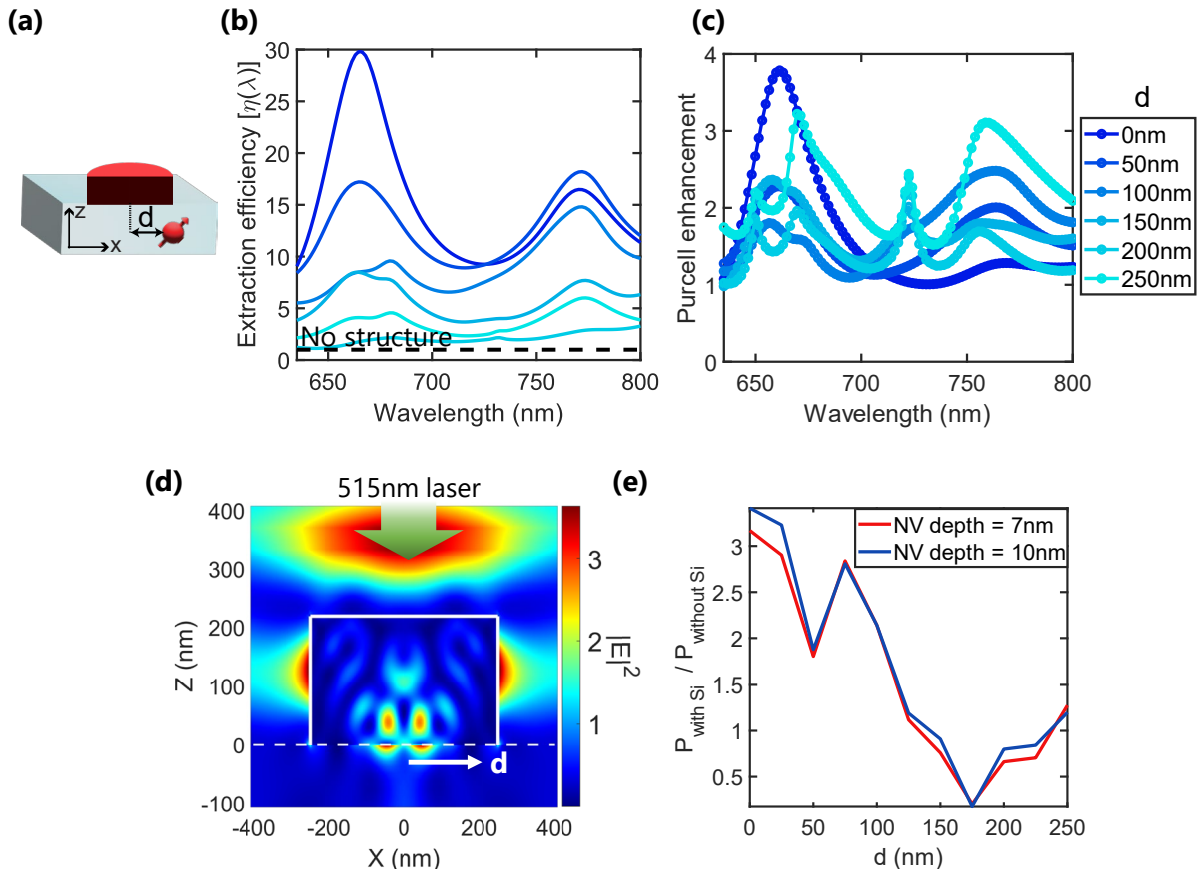

Figure S4. (a) Schematic of the misalignment of the Si antenna and NV center within 10 nm of the surface in the x-direction. (b) Simulated extraction efficiency [η(λ)] of the Si antenna as a function of NV center misalignment, ranging from 0 nm to 250 nm. (c) Purcell enhancement of the Si antenna relative to the x-location of the NV center. (d) Snapshot of the electric field (E-field) distribution when a 515 nm laser passes through the Si antenna and diamond. (e) Simulated laser power perceived by NV centers located 7 nm and 10 nm below the surface when illuminated by a 515 nm laser.

Since we did not align NV center and Si antenna during e-beam lithography, some location mismatching occurred (Fig. S4(a)). To simulate the potential misalignment of the NV center in the +x direction, we performed finite-difference time-domain (FDTD) simulations (Ansys Lumerical FDTD), considering the circular shape of the antenna. Fig. S4(b) and Fig. S4(c) show the NV center's position along the x-axis, ranging from 0 nm (aligned) to 250 nm (at the edge of the pillar), with the NV center depth fixed at 10 nm. The extraction efficiency (Fig. S4(b)) decreases with increasing misalignment, and the Purcell enhancement (Fig. S4(c)) exhibits resonance shifts at different wavelengths. Additionally, no significant difference was observed between the P_{sat} values of both samples (with and without the antenna) when illuminated with a 515 nm green laser. There are hot spots between x = –100 nm and x = +100 nm down to a depth (Z) of 10 nm (Fig.

S4(d)), suggesting that NV centers in diamond with Si antennas may be affected by this. Fig. S4(e) shows the laser power perceived by NV centers located 7 nm and 10 nm below the surface. The experimentally measured P_{sat} of the NV center in the bare diamond is ~2.4 mW, while the experimentally measured P_{sat} of the NV center with the Si antenna is ~2.1 mW. Considering the measured fluorescence count rates from the Si pillar, the simulated extraction efficiency as a function of NV displacement, measured reduction in lifetime, and the P_{sat} ratio, we conclude that the NV center beneath the Si pillar in our measurement is laterally displaced by 150–200 nm.

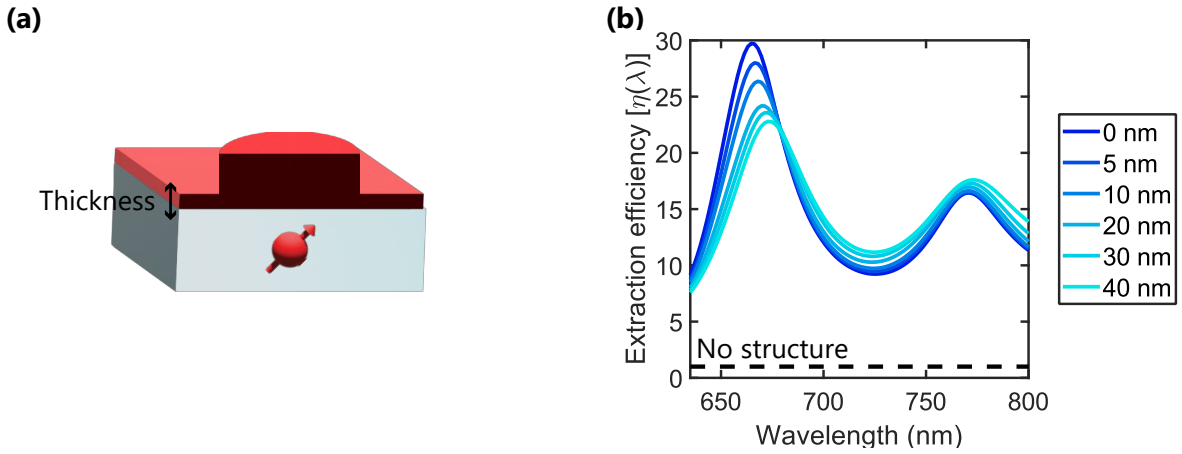

Figure S5. (a) A schematic of the under-etching the silicon (Si) membrane on top of the diamond with a Si antenna. (b) Simulated extraction efficiency [η(λ)] of the Si antenna as a function of the remaining thickness of the Si membrane atop the diamond.

Since O_2 plasma etches diamond[31] and we are using shallow NV centers (~10 nm), we aimed to protect the diamond surface from the plasma exposure. To achieve this, we attempted to under-etch the Si membrane on top of the diamond (Fig. S5(a)). Fig. S5(b) shows that there is no significant difference in extraction efficiency between a fully etched Si membrane (0 nm) and an under-etched Si membrane (~40 nm).

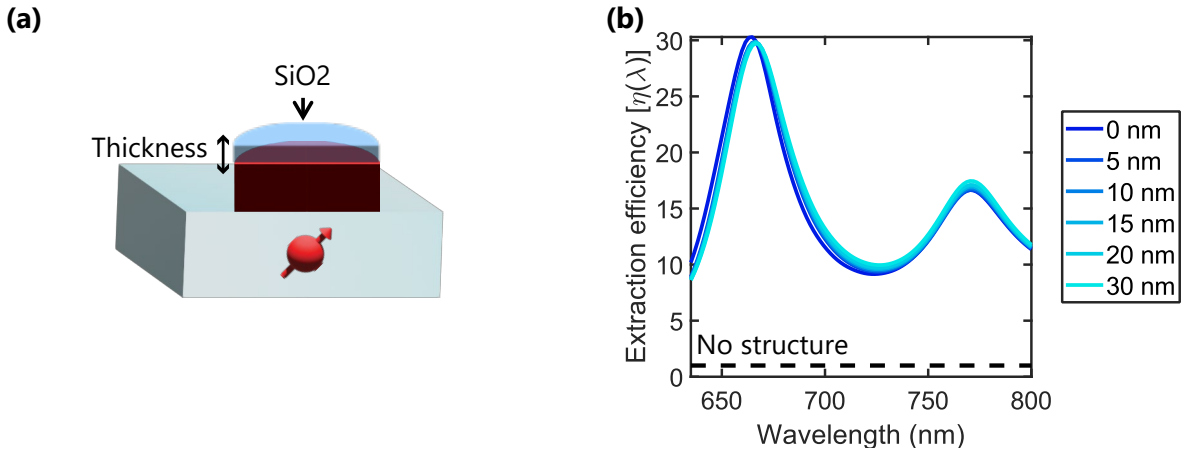

Figure S6. (a) A schematic of the SiO_2 hard mask on top of the Si antenna. (b) Simulated extraction efficiency [η(λ)] of the Si antenna as a function of the remaining thickness of the SiO_2 hard mask.

To define the circular shape of Si antenna, we used an SiO_2 hard mask as the etch mask (Fig. S6(a)). After etching, some SiO_2 remained on top of Si antennas. We chose to not remove this layer, because it is not expected to affect the optical properties due to its low index (refractive index n ~ 1.45) and small thickness. This is confirmed in the simulations of extraction efficiency as a function of the SiO_2 layer on top (Fig. S6(b)).